High-precision relocation and focal mechanism of the 2002 rain-triggered earthquake swarms at Mt. Hochstaufen, SE-Germany

High-precision relocation and focal mechanism of the 2002 rain-triggered earthquake swarms at Mt. Hochstaufen, SE-Germany

T. Kraft[1], J. Wassermann[1] and H. Igel[1]

[1]*Ludwig-Maximilians University, Department of Earth and Environmental Sciences, Geophysics Section,*

Theresienstr. 41, 80333 Munich, Germany

Kraft@LMU.de, Jowa@LMU.de, Heiner.Igel@LMU.de

SUMMARY

The 2002 seismicity of Mt. Hochstaufen, SE-Germany, is characterized by several swarm-type earthquake sequences that follow above average rainfall events. First investigations have recently provided indication, that the rain events triggered this swarm-type activity. We present a detailed relocation of the 2002 seismicity, which is composed of (1) cluster analysis, (2) multi-event semi-automatic phase repicking, (3) probabilistic location in a pseudo-3D-velocity model with topography and (4) master event relocation. Furthermore, focal mechanisms of selected events are derived by taking into account the first-motion polarities of P, SV and SH-waves. We introduce a simple methodology to test the stability and estimate the variance of the focal mechanisms solutions.

Location uncertainties of less then one hundred meters were achieved. The hypocenters are mainly concentrated between 1000m above and 4000m below sea level and aligned on two planes, which, however, can not be associated with geological structures with reasonable certainty. Swarm-type activity follows above average rain events and shows a depth migration of hypocenters over time. Evidence that the rain events triggered the earthquake swarms is reported by Hainzl et al. (2006) on basis of our relocation. The

2   *T. Kraft et al.*

derived focal mechanisms seem to indicate an influence of the Saalachtal Fault Zone on the stress regime of the study area.

Key words: microearthquake swarm – rainfall-triggered seismicity – cluster analysis – probabilistic non-linear inversion – master event relocation – focal mechanism determination

1   INTRODUCTION

Observations of several decades indicate, that the seismicity of the Staufen Massif, SE-Germany, is influenced by meteorological parameters, i.e. the longtime record of annual variation of seismicity and precipitation are well correlated (Schwarzmann et al., 2001). A further characteristic of the area is the occurrence of earthquake swarms that seem to follow above average rainfall events. In 2002, a newly installed permanent seismological network recorded several complete swarm-type earthquake sequences, which followed above average rain events. Based on first results of their analysis of this data set, Kraft et al. (2005) recently suggested reduction of frictional fault strength due to increase of pore pressure caused by diffusion of rain water to seismogenic depths as causative mechanism.

The spatial and temporal distribution of earthquakes can provide information on the tectonic regime and the material properties of an area. However, precise earthquake hypocenter locations are required to study the processes that trigger seismic activity. Location results of the 2002 Mt. Hochstaufen seismicity were until now based on manually determined absolute arrival times, a homogeneous half-space velocity model derived by joint hypocenter-velocity inversion and a location algorithm not taking into account the rough topography of the study area.

Improvement of the precision and reliability of earthquake locations can be achieved by adapting the velocity model to better represent the actual geological and topographic setting of the study area. Yet, the majority of available location algorithms uses layered velocity models and only account for lateral variations in velocity and topography by introducing static station corrections. These corrections represent an average of observed travel-time residuals for seismic waves arriving from spatially distributed sources. This means, that they can not correctly represent azimuthal variations of the seismic velocities. On the other hand, such algorithms are not able to take advantage of the three-dimensionality of the station distribution in rough topography, and to decide whether shallow hypocenters are located above or below the mean station elevation. We overcome the afore mentioned drawbacks by using a pseudo-3D-velocity model with high-resolution topography and a probabilistic, non-linear earthquake location method, originally formulated by Tarantola & Valette (1982). An additional major advantage of this method is that it provides complete description of the location uncertainty estimates.

Relocation and focal mechanisms of rain-triggered earthquake swarms 3

We can further improve the location accuracy by applying cross-correlation techniques to identify groups of events with very similar waveforms and derive highly accurate relative phase-onset times. Very similar wave forms of different events recorded at one station indicate that the hypocenters and focal mechanisms are nearly identical (e.g., Geller & Mueller, 1980). It is therefore possible to use the master-event technique to calculate relative earthquake locations for a group of similar events with respect to a master event with high accuracy. Absolute earthquake location can than be calculated from the solution of the probabilistic, non-linear earthquake location for the master event.

The fault-plane orientations and slip directions of earthquakes can provide important information about fault structure at depth and the stress field in which the earthquakes occur (e.g., Gephart & Forsyth, 1984). Reliable fault-plane solutions can be obtained by observing the first-motion polarities of the P-wave, when many observations with good azimuthal coverage are available. In a less denser station network additional information can be gained by analyzing the first-motion polarity of SV and SH-component of the S-wave in three-component seismograms. However, the stability of the obtained focal mechanisms has to be carefully tested. We introduce an algorithm similar to that proposed by Hardebeck & Shearer (2002) for pure P-polarity datasets and test the stability of the focal mechanism solution by accounting for wrong polarity readings.

2 STUDY AREA AND DATA

The Staufen Massif is situated at the northern margin of the Alps near the town Bad Reichenhall in SE Germany (Fig. 1). It belongs to the elongated fold-and-thrust belt of the Northern Calcareous Alps (NCA) and its geology is dominated by lower to middle Triassic limestone and dolomite with bedding planes dipping $60°$ to the south, approximately. The Staufen Massif builds a part of the thrust front of the NCA onto the Flysch Zone, a sequence of shales rhythmically interbedded with sandstones. This east-west striking geological border at the northern foot of the mountain chain is also characterized by a prominent contrast of seismic velocities. In the south the Saalachtal Fault Zone (SFZ), a major sinistral strike-slip zone with an offset in the order of 12–15 km, primarily active in late-Oligocene and Miocene time (Frisch & Gawlick, 2003), separates the Staufen Massif from the topographic low of the Reichenhall Basin with salinar sequences of remarkable thickness, which explain the increased mobility of the tectonic units in the region. A schematic tectonic map of the study area is shown in Figure 1.

Further, geologic evidence for mass movements at the southern flank of Mt. Hochstaufen was recently summarized by Weede (2002). Large east-west striking open fractures near the summit of Mt. Hochstaufen reach a length of several hundred meters, openings of up to three meters and depths of at least hundred meters. Gravitational collapse and/or subsidence due to leaching of the Haselgebirge forma-

4   *T. Kraft et al.*

tion, an evaporitic breccia, are debated as causative processes.

Observations of several decades indicate, that the seismicity in this area is influenced by meteorological parameters, i.e. the longtime record of annual variation of seismicity and precipitation correlate well (Schwarzmann et al., 2001). A further characteristic of the area is the occurrence of earthquake swarms that seem to follow above average rainfall events. The seismicity is mainly concentrated on the Staufen Massif, whereas the surrounding is characterized by relative low seismic activity.

Starting in 2001 a permanent seismological network was installed in the area of Mt. Hochstaufen to study this phenomenon in detail. The network consists of six permanent and three mobile stations equipped with short-period three-component seismometers. Additionally, data of four pluviometers and several ground-water wells around the Staufen Massif are available (refer to Kraft et al. (2005) for details). A location map of all stations is shown in Figure 2.

In March and August 2002, intense rainfall events led to severe flooding in Central Europe, causing an economic damage of 18.5 billion Euro (Munich Re Group, 2003). Precipitation in the study area exceeded the monthly average within 48h, respectively 24h, during these events. As illustrated in Figure 3 the seismicity in the Staufen Massif increased significantly after both rain events. It rose roughly coincident with the onset of the intense rain. In both cases seismicity reached its maximum approximately ten days after the onsets and stayed on an elevated level for several weeks.

In 2002, a total of 1171 earthquakes was recorded in the study area. The strongest event had a magnitude of Ml=2.4 on April 10. The magnitude-frequency statistic follows the Gutenberg-Richter law with a typical b-value of 1.1 $\pm$0.1 for magnitudes larger than Ml=-0.2. Below this value the distribution deviates from the Gutenberg-Richter law indicating incomplete data collection. The seismicity is very shallow and rarely exceeds 3km (b.s.l.). Swarm-type seismicity phases can be identified, which follow the intense rain events in March and August. The August swarm can further be divided in at least three subswarms (Kraft et al., 2006).

The seismological data set consists of several families of earthquakes characterized by very similar wave forms. This indicates that these events have nearly identical hypocenter locations and focal mechanisms. Several techniques exist, which take advantage of wave-form similarity to compute highly accurate relative earthquake locations (e.g., Aster & Rowe, 2000, and references therein). We use a combination of those techniques to identify clusters of similar events and to reduce location uncertainty in the data set.

3   CLUSTER ANALYSIS

Small earthquakes that are characterized by very similar waveforms recorded at the same station should only be separated by distances less than a quarter of their dominant wavelength (e.g., Geller

& Mueller, 1980). Hence, in order to identify groups of closely spaced earthquakes in the data set, waveform similarity served as a measure of hypocenter proximity in a hierarchical cluster analysis, which will be outlined in the following.

For every earthquake time windows of length 7 s starting 1 s before the P-onset were extracted from the vertical component records of station STAU, which was the station that recorded the most events of the 2002 data set (Kraft et al., 2006). Further, we applied a bandpass filter (3 - 20 Hz) and cross-correlation to quantify the similarity of different seismograms using the GIANT analysis system (Rietbrock & Scherbaum, 1998). The resultant set of maximum cross-correlation coefficients c_{ij} for every possible combination of events $i, j \in [1, N]$ (N = 1171 = number of events) were arranged to form a square symmetric similarity matrix $\mathcal{C}$. A visualization of the similarity matrix $\mathcal{C}$ is shown in Figure 4a. The shape of $\mathcal{C}$ can be interpreted as follows: (1) Squares representing sets of highly similar events are aligned on the diagonal, indicating that similar events are as well clustered in time. (2) Off-diagonal rectangular areas partly link the main-diagonal squares, suggesting reactivation of seismogenic regions over time. (3) Some main-diagonal squares spanning a range of low event numbers seem only be weakly linked to other elements, indicating a concentration of seismicity to a different source region in the corresponding time period. This interpretation is supported by the results of Kraft et al. (2005) , which found that the March swarm was located further south and deeper than most of the remaining seismicity in 2002.

The similarity matrix $\mathcal{C}$ built the basis of a hierarchical cluster analysis, where in an iterative process similar entities (events or groups of events represented by the relevant rows and columns of $\mathcal{C}$) were repeatedly joined to form a hierarchical tree, beginning by merging the most similar waveforms. The similarities between the newly formed group and all other entities were calculated using the pairwise single linkage technique (e.g., de Hoon et al., 2004), where the similarity between two entities was defined as the highest similarity among the pairwise similarities between their members. The joining process was repeated until a user-defined lower similarity threshold of $c_{ij} \geq 0.8$ was reached.

In total 145 clusters were identified, with a minimum of two and up to 16 members. Figure 4b+c illustrate how many and which events were joined to form clusters. Seismogram examples of representative clusters of the March swarm (CL024) and the August swarm (CL011 and CL014) are shown in Figure 5. Even though, only the vertical component (Z) was considered in the cluster analysis, cluster members are characterized by having very similar wave forms also in the horizontal components. Although, the magnitudes can range from Ml=-0.8 to Ml=1.6 inside the clusters (e.g., CL014), the similarity is preserved over the complete length of the seismograms. This indicates that for the observed magnitude range, the waveforms are nearly independent of the source-time function and are predominantly influenced by the Green function of the medium and the focal mechanisms. However,

6   *T. Kraft et al.*

because of the high waveform similarity the latter two seem to be nearly identical within a cluster. This motivates and justifies the methodology described in the following.

4   MULTI-EVENT SEMI-AUTOMATIC PHASE REPICKING

Comparing similar waveforms can provide highly accurate relative phase arrival times. Thereby, the time difference between the arrivals of the same phase at one station for different earthquakes is derived by cross-correlation in the time or in the frequency domain (e.g., Poupinet et al., 1984; Deichmann & Garcia-Fernandez, 1992). However, these relative arrival times have to be related to some master phase onset determined from single event picking when absolute arrival times are desired. Yet, the accuracy of onset times determination can be significantly improved when comparing a number of similar phase-aligned seismograms simultaneously (Rowe et al., 2002).

We performed a multi-event semi-automatic phase repicking within the clusters identified beforehand. Seismograms of all cluster members were component-wise aligned with respect to the event with the largest magnitude (master event) using the analysis software Seismic Handler (Stammler, 1993). All seismograms were than phase-wise cross-correlated with the master event and realigned for the time lag corresponding to the maximum cross-correlation coefficient cc_{ij}. The window lengths for this correlations was chosen interactively, assuring the alignment of even noisy seismograms. If necessary, the master phase onset time was corrected manually. The slave phase-onset times were calculated by adding the cross-correlation derived time differences to the time of the master phase-onset. Phase weights were derived by incrementing the picking weight obtained for the master-event phase according to the value of cc_{ij} as listed in Table 1.

We checked the derived onset times by calculating arrival-time differences of P-phases and S-phases (dt_p and dt_s) with respect to station STAU for every event and available station. Within one cluster these arrival-time differences for one station should be nearly identical. Further, the ratio dt_s/dt_p should correspond to the ratio of the seismic velocities (v_p/v_s). Events that violated these criteria were excluded from further analysis. After this selection 51 clusters with $\max\{dt_p, dt_s\} \leq 0.03$ s remained. Figure 6 shows a normalized cumulative histogram of the 314 standard deviations $\sigma^{cl}(dt_p, dt_s)$ derived from the sets of dt_p and dt_s. The 95%-level is indicated by a dash-dotted line and demonstrates that $\sigma^{cl}(dt_p, dt_s) \leq 0.012$ s holds for over 95% of the data. This indicates a very good agreement of the phase-arrival times of different events of one cluster at the individual stations.

Encouraged by this fact, we calculated synthetic phase-arrival times for missing stations of individual cluster members. This was done by adding $dt_{p,s}$, derived for the master event, to the phase arrival time at station STAU of the corresponding event. Weights for these synthetic phases were calculated by increasing the master phase weight by two (comp. Table 1). In this way we assured that the location

Relocation and focal mechanisms of rain-triggered earthquake swarms   7

uncertainties derived for events with synthetic arrival times were adequately high. Using this procedure, the number of locatable earthquakes was increased from 546 to 612.

5   EARTHQUAKE RELOCATION

5.1   PROBABILISTIC EARTHQUAKE LOCATION

Based on the data set described above, we calculated probabilistic locations for Mt. Hochstaufen earthquakes using the software package NonLinLoc (Lomax et al., 2000). As the study area is characterized by a strong north-south velocity contrast and a rough topography, we composed the velocity model of two homogeneous quarter-spaces with realistic topography. Compressional seismic wave velocities (v_P) were taken from seismic refraction studies in the Eastern Alps (Will, 1975; Bleibinhaus & Gebrande, 2006). A typical velocity for the Flysch Zone ($v_P = 3.6$ km/s) was assigned to the northern part of the model, whereas $v_P = 5.8$ km/s, typical for the Northern Limestone Alps (NCA), was used in the southern part. Above the topography, which was taken from a 50×50 m digital elevation model provided by the Geodetic Survey of the Bavarian State (LVG-Bayern, 2000), the velocity was set to $v_P = 10^{-6}$ km/s. This was necessary, because a slowness model had to be specified for input in NonLinLoc. For conversion from compressional to shear wave velocity model the ratio $v_p/v_s = 1.81$, derived in a previous study (Kraft et al., 2006), was used. The velocity model was discretized with a grid spacing of 100 m. The model dimensions and the geographical setting are given in Figure 7.

The location algorithms implemented in NonLinLoc follows the probabilistic formulation of inversion and the equivalent methodology for earthquake location (e.g., Tarantola & Valette, 1982; Moser et al., 1992; Wittlinger et al., 1993; Lomax et al., 2000). Tarantola & Valette, (1982) showed, that the complete probabilistic solution to the inverse problem can easily be expressed as a posteriori probability density function (PDF) in an easy way, if the calculated and the observed arrival times are assumed to have Gaussian uncertainties expressed by covariance matrices (C_T and C_d in Tarantola, 2004, p. 35), and if the a priori information on the origin times is taken as uniform. This assumption allows a direct, analytical evaluation of the PDF for the spatial location and the origin time as well as comprehensive uncertainty and resolution information. A complete description of the underlying theory can be found in Tarantola (2004).

For every station of the 2002 Mt. Hochstaufen network theoretical travel times to all grid points of the velocity model were calculated using a Huygens-principle finite-difference algorithm (Podvin & Lecomte, 1991). We used the nested grid search algorithms, implemented in NonLinLoc, to obtain the PDF, which represents the complete probabilistic spatial solution to the earthquake location prob-

8   *T. Kraft et al.*

lem. The PDF indicates the uncertainty in the spatial location due to Gaussian picking and travel-time calculation errors as well as the network–event geometry. The maximum-likelihood point of the complete, non-linear location PDF was selected as the hypocenter solution and Gaussian error estimates were calculated by Singular Value Decomposition (SVD) of the combined covariance matrixes ($C_D = C_T + C_d$, Tarantola, 2004, p. 35).

In Figure 8 four examples for a posteriori probability density functions are given. The PDFs are scaled to have unit probability when integrated over the final search grid (horizontal: 5×5 km; vertical: 7 km). A typical event of the March swarm (Figure 8a) and the master event of cluster CL024 as a typical event of the August swarm (Figure 8b) represent examples of good location results. All but one Stations (RTBE) contribute to the solution. The PDF are of elliptical shape and have a strong maximum resulting in small confidence volumes. The largest event of 2002 on April 10 reaching a magnitude of Ml=2.4 is unfortunately an example for a badly confined event (Figure 8c). Resulting from the lack of mobile stations and down-weighted arrival-time picks of remote stations the especially the depth has a large uncertainty.

For some events that only had few arrival-time readings of low quality a second maximum of the PDF can develop above the surface as shown in Figure 8d. This is due to the fact, that the volume above the topography can absorb uncertainties in the input data because of its very low velocity. The super-topographic maximum sometimes dominated the PDF and lead to wrong location results. Therefore, events of this kind were excluded from further analysis.

Figure 9 illustrates the quality of the location result in form of normalized histograms of the root mean square residual of calculated to observed arrivaltimes (RMS) and estimated Gaussian confidence intervals of hypocenter location (erh and ehz, representing lateral and vertical uncertainty) . For 90% of the 612 located events location uncertainties are smaller than 0.7 km and the RMS less than 0.12 s. For 75% of the data are ehz<0.4 km, erh≤0.6 km and RMS<0.1 s. This indicates that for the great majority of events the absolute location are already of good quality. In the following we will take advantage of the results of the cluster analysis and calculate relative location of all cluster members with respect to their master events.

5.2   MASTER EVENT LOCATION TECHNIQUE

The master-event location technique, as all multiple-event location procedures, assumes that if the hypocentral separation between a set of earthquakes is small compared to the event-station distance and the scale length of heterogeneity, then the ray paths between a source region and a station are similar and the error introduced by incorrect assumptions regarding velocity structure has a nearly constant value for times measured at the same station (e.g., Wolfe, 2002).

The cluster analysis described above has identified 143 clusters of at least two similar events. Within these clusters we expect the conditions for master-event locations to be fulfilled when excluding stations that are too close to the hypocenters. This can easily be achieved by choosing a lower threshold for the arrival-time difference of P- and S-phase (dt_{sp}) at a station. To assure a minimum event-station distance of 2 km this threshold was set to $dt_{asp} = 2\text{ km} * (v_p/v_s - 1)/v_P \geq 0.28$ s, using v_P=5.8 km/s and v_P/v_S=1.81.

The governing equation for master-event location can be derived from the geometrical setting shown in Figure 10. The relationship between the arrival-time differences of a phase (P or S) from master event (M) and the same phase from the slave event (S_j) at station i can be expressed as:

$$^i dt_{p,s}^{S_j} = \Delta T^{S_j} - \frac{\mathbf{L}^{S_j} \cdot {}^i\mathbf{n}^{S_j}}{v_{p,s}} \tag{1}$$

Where ΔT^{S_j} is the difference in origin time between master and slave event, $\mathbf{L}^{S_j}$ and ${}^i\mathbf{n}^{S_j}$ are the vectors defined in Figure 10, and $j \in [1, k_c]$ and $i \in [1, l_c]$ with k_c and l_c the cluster-specific numbers of slave events and observing stations.

For every master-slave event pair of a cluster $2l_c$ equations for $^i dt_{p,s}^{S_j}$, weighted by the cross-correlation coefficient cc_{MS_j} (comp. Section 4) obtained for the corresponding events and phases (e.g., Waldhauser & Ellsworth, 2000), were combined in linear systems of the form:

$$\mathbf{d}^{S_j} = \mathcal{G}^{S_j} \cdot \mathbf{m}^{S_j} \tag{2}$$

Taking a closer look at one master-slave pair, the data vector $\mathbf{d}^{S_j}$, model vector $\mathbf{m}^{S_j}$ and matrix $\mathcal{G}^{S_j}$, when dropping the super-script S_j and sub-script c for brevity, expand to:

$$\begin{pmatrix} ^1dt_p \\ ^1dt_s \\ \vdots \\ ^ldt_p \\ ^ldt_s \end{pmatrix} = \begin{pmatrix} 1 & -\frac{^1n_x}{v_p} & -\frac{^1n_y}{v_p} & -\frac{^1n_z}{v_p} \\ 1 & -\frac{^2n_x}{v_s} & -\frac{^2n_y}{v_s} & -\frac{^2n_z}{v_s} \\ \vdots & \vdots & \vdots & \vdots \\ 1 & -\frac{^ln_x}{v_p} & -\frac{^ln_y}{v_p} & -\frac{^ln_z}{v_p} \\ 1 & -\frac{^ln_x}{v_s} & -\frac{^ln_y}{v_s} & -\frac{^ln_z}{v_s} \end{pmatrix} \cdot \begin{pmatrix} \Delta T \\ x \\ y \\ z \end{pmatrix}$$

Within one cluster the linear systems for the k_c master-slave event pairs can be combined to one system of the form:

$$\begin{pmatrix} \mathbf{d}^{S_1} \\ \mathbf{d}^{S_2} \\ \vdots \\ \mathbf{d}^{S_{k_c}} \end{pmatrix} = \begin{pmatrix} \mathcal{G}^{S_1} & \mathcal{O} & \cdots & \mathcal{O} \\ \mathcal{O} & \mathcal{G}^{S_2} & \cdots & \mathcal{O} \\ \vdots & \vdots & \ddots & \vdots \\ \mathcal{O} & \mathcal{O} & \cdots & \mathcal{G}^{S_{k_c}} \end{pmatrix} \cdot \begin{pmatrix} \mathbf{m}^{S_1} \\ \mathbf{m}^{S_2} \\ \vdots \\ \mathbf{m}^{S_{k_c}} \end{pmatrix}$$

which will briefly be referred to as

$$\mathbf{d}^{MS} = \mathcal{G}^{MS} \cdot \mathbf{m}^{MS} \tag{3}$$

10 *T. Kraft et al.*

Using Matlab® (2005), these linear systems were solved by calculating the generalized inverse (Moore, 1920; Penrose, 1955) $(\mathcal{G}^{\mathrm{MS}})^{+}$ of $\mathcal{G}^{\mathrm{MS}}$ and assessing the optimal estimate of $\mathbf{m}^{\mathrm{MS}}$ in a least square sense by computing

$$\mathbf{m}_{\mathrm{est}}^{\mathrm{MS}} = (\mathcal{G}^{\mathrm{MS}})^{+} \cdot \mathbf{d}^{\mathrm{MS}} \tag{4}$$

Under the assumption that the data are uncorrelated and have equal variance σ_d^2, error estimates for the relocated slave events can be derived by plugging $\mathbf{m}_{\mathrm{est}}^{\mathrm{MS}}$ into Equation 3 to obtain an estimate of the data vector $\mathbf{d}_{\mathrm{est}}^{\mathrm{MS}}$, and calculating the sample variance s as an estimate of the true data variance σ_d^2 (e.g., Menke, 1989):

$$s = \frac{1}{2l_c - 4}(\mathbf{d}_{\mathrm{est}}^{\mathrm{MS}} - \mathbf{d}^{\mathrm{MS}})^2 \tag{5}$$

An estimate for the model co-variance matrix $\mathcal{S}_{m_{\mathrm{est}}}^2$ can than be obtained from:

$$\mathcal{S}_{m_{\mathrm{est}}}^2 = \sigma_{d_{\mathrm{est}}}^2 \cdot ((\mathcal{G}^{\mathrm{MS}})^T \cdot \mathcal{G}^{\mathrm{MS}})^{-1} \tag{6}$$

Master-event relocations for representative clusters are shown in Figure 11. Unfortunately the estimated errors are of comparable size as the distances between master and slave events. This prohibits a detailed interpretation of the geometrical distribution of the events within a cluster. However, the size of the event clouds seems to be a good estimate of the volume occupied by the cluster. For events with relocation uncertainty smaller then 200 m absolute locations were derived by adding the relative location and the NonLinLoc-location. For larger uncertainties of the master-event location we regard the NonLinLoc-location as more reliable. However, the master-event relocation significantly reduced the spread of the earthquake clouds compared to the probabilistic result down to a size of a few meters.

5.3 RESULT OF THE RELOCATION

Hypocenters obtained using the master-event location technique were combined with the results of the probabilistic inversion to form the solution data set. If the location uncertainty of a relative location was less than 200 m the corresponding absolute location was included in the solution data set, otherwise the result of the probabilistic inversion were used. Compared to previous hypocenter locations, where the seismicity was diffusely distributed below the Staufen Massif (Figure 12a, comp. Kraft et al., 2006), spatial and temporal patterns can now clearly be identified in the seismicity (Figure 12b+c).

Using a pseudo-3D-velocity model with topography allowed to identify events above the average station elevation by taking advantage of the three-dimensionality of the station distribution. Hence, the depths of the located hypocenters span a range between -1.7 km and 4.2 km (b.s.l.) with the majority of the events deeper than -1.0 km. This means that earthquakes in the Staufen Massive can occur more

than 1000m above the Reichenhall Basin.

In March 2002, the swarm-type seismicity concentrates in a very small source volume in 3 km depth south of Mt. Hochstaufen (Figure 12b+c). The relocation tightened the hypocenter cloud significantly and in particular reduced its depth extension. The source volume of the March swarm coincides with the surface trace of the Kugelbach Zone, a part of the sinistral Saalachtal Fault Zone (Figure 1).

Later in the year, mainly during the swarm sequences starting in August, the seismicity is distributed over a lager source volume inside the Staufen Massif. However, the hypocenters seem to align along two planes. One is striking north-south and dipping approximately 50° west, connecting the easternmost summit of the Staufen Massif, and the source volume of the March swarm (comp. east-west cross-section in Figure 12b). Yet, the strike and dip do not correspond to geological features observed in the study area and no explanation for the alignment along this plane can be given at present. The second plane seems to strike east-west with a southern dip of approximately 10°, very shallow beneath the mountain chain. Although, the thrust fault and the bedding plane orientations in the Staufen Massif follow this trend in general, the observed dip of the seismicity is to shallow to be associate it with these geological features with reasonable certainty.

The spatio-temporal development of the seismicity (Figure 12c) is essential the same as before the relocation and was described in detail by Kraft et al. (2006). A major feature that can be observed is the concentration of earthquakes in several swarm-type sequences, which follow above average rain events. Furthermore, the August earthquake swarm is characterized by a depth migration of hypocenters over time. On the basis of these observations, Kraft et al. (2006) proposed that rainfall triggered the earthquakes via the mechanism of pore pressure diffusion. Evidence for this hypothesis was recently reported by Hainzl et al. (2006) , successfully predicting the seismic event rate from the calculated pore-pressure change at depth due to rainfall.

6 FOCAL MECHANISM DETERMINATION

The fault-plane orientations and slip directions of earthquakes can provide important information about fault structure at depth and the stress field in which the earthquakes occur (e.g., Gephart & Forsyth, 1984). The source of a small earthquake is typically approximated by a double-couple point source derived from observed body-wave first-motion polarities. The nodal planes of the body-wave radiation pattern excited by a point source divides a reference sphere around the source into areas of opposite first-motion polarities. The polarities can either be away from or toward the source for P-waves, away from or toward the source for the SV-component of the S-wave and to the left or to the right looking from the source for the SH-component of the S-wave (e.g., Pujol, 2003). The first-motion polarities, observed at the seismic stations, are projected to the focal sphere at the azimuth and takeoff

12   *T. Kraft et al.*

angle at which the seismic ray leaves the source. A focal mechanism can then be found that best fits the first-motion observations.

A widely used method for determining first-motion focal mechanisms from P, SV and SH-polarity data is the FOCMEC software package (Snoke, 2003). FOCMEC employs a grid search over all possible fault-plane orientations to identify the best-fitting focal mechanism and reports acceptable solutions based on selection criteria for the number of polarity data errors. However, no quality estimate for the solution is given and no stability check is performed in FOCMEC. We introduce an algorithm similar to that proposed by Hardebeck & Shearer, (2002) for pure P-polarity datasets and test the stability of the focal mechanism solution by accounting for wrong polarity readings.

After applying a bandpass filter of 3-15 Hz the 3-component seismograms were rotated into the ray coordinate system to separate the P, SV and SH-components. The azimuth and incidence angles of the ray, needed for this rotation, were derived by a polarization analysis of the three-component recording of the P-onset. First-motion polarities were then determined in the rotated seismograms for all clusters and all events with more than five recording stations. The event clusters where treated as single events by combining the polarity information taken form seismograms of stations which had the highest signal to noise ratio. This was justified by the high similarity of the wave forms of the cluster members and by the fact that they coincide within the accuracy of the master event location technique.

FOCMEC was used to find the best fitting focal mechanism. The polarities were weighted according to the radiation pattern allowing for an absolute polarity error of two. Additionally, for all events and clusters N further FOCMEC runs where done with the same error tolerance, but each time leaving out one of the N polarity observations. Between one and fifty acceptable focal mechanisms were found for each run. Following the algorithm of Hardebeck & Shearer, (2002) we calculated a preferred focal mechanism by vectorial averaging the normal vectors of the fault and auxiliary fault plane separately. Furthermore, we where in this way able to derive an estimate for the variance of the two normal vectors. Figure 13 shows the perferred focal mechanisms of 25 events with at least 12 polarity observations and a maximum normal vector variance of $20°$.

The preferred mechanisms of the nine clusters and 16 single events are plotted in an epicenter map scaled by magnitude and depth in Figure 14a. Three different faulting regimes, indicated by ellipses, seem to exist in the study area: (A) reverse faulting in the south-eastern part of Mt. Hochstaufen, (B) normal faulting in the central part of the Staufen Massif and (C) sinistral strike-slip faulting south of the massif near to the surface trace of the Saalachtal Fault Zone (SFZ, Figure 1+14a). The number of derived focal mechanisms is not sufficient to give a definite answer to the question which tectonic processes control the seismicity of the Staufen Massif. However, the observed faulting regimes could indicate, that the SFZ is still active (C), forms a restraining bend in the south-east of the Staufen Mas-

Relocation and focal mechanisms of rain-triggered earthquake swarms 13

sif (A) and further leads to extension of the central part of mountain chain (B). If this interpretation, which is illustrated in Figure 14b, is valid has to be carefully tested in the future and has a major impact on seismic hazard assessment.

7 DISCUSSION

We have relocated 612 earthquakes of the 2002 Mt. Hochstaufen seismicity. By cross-correlation based cluster analysis 145 groups of similar earthquakes with up to 16 members were identified. Highly similar events are partly also clustered in time and reactivation of seismogenic regions over time occurs. However, the seismicity is concentrated in different source regions in the beginning and end of 2002. Even though only the vertical component was considered in the cluster analysis, cluster members are characterized by having very similar wave forms also in the horizontal components. Furthermore, the high similarity is preserved over the complete length of the seismograms, even though, the strength of the earthquakes within a cluster can span two magnitudes. This indicates that for the observed magnitude range, the waveforms are nearly independent of the source-time function and are predominantly influenced by the Green function of the medium and the focal mechanisms. However, because of the high waveform similarity the latter two seem to be nearly identical within a cluster.

For all identified clusters a multi-event semi-automatic phase repicking improved the accuracy of onset-time determination. By taking advantage of the simultaneous display of all cross-correlation aligned one-component seismograms. Phase onsets where in this way identified more easily by tracking consistent wave forms over several traces. A quality check of the onset times demonstrated high consistency between individual cluster members with a standard deviation of relative arrival-time differences of $\sigma^{cl} \leq 0.012$ s.

The absolute hypocenter location, calculated by a probabilistic non-linear method using the software package NonLinLoc (Lomax et al., 2000), are of good quality. This is indicated by location uncertainties smaller than 0.6 km and root mean square (RMS) residuals of less then 0.1 s for the majority of the events (75%). Relative locations with respect to the strongest event of a cluster were derived using the master-event technique. Unfortunately, the estimated errors are of comparable size as the obtained distances between master and slave events. This prohibits a detailed interpretation of the geometrical distribution of the events within the clusters. The master-event relocation significantly reduced the dimensions of the earthquake clouds compared to the probabilistic result down to a size of a few meters. Compared to previous location results, where the seismicity was diffusely distributed below the Staufen Massif (Kraft et al., 2006), spatial and temporal patterns in the seismicity can now be clearly identified. Earthquake hypocenters were located in a depth range between -1.7 km to 4.2 km (b.s.l.) with the majority of events deeper than -1 km, which means that earthquakes in the Staufen Massive can

occur more 1000 m above the Reichenhall Basin. During the March swarm sequence, the seismicity mainly concentrates in a very small source volume in 3 km depth south of Mt. Hochstaufen, which coincides with the surface trace of the sinistral Saalachtal Fault Zone. Later in the year, mainly during the swarm sequences starting in August, the seismicity is distributed over a lager source volume inside the Staufen Massif. Hypocenters seem to align along two planes. One striking north-south and dipping west, the second plane strikes east-west with a nearly horizontal southern dip very shallow beneath the mountain chain. Neither of the planes can with reasonable certainty be associated with geological features observed in the study area.

Further, we have combined the focal-mechanism determination based on first-motion polarities of P and S-waves (Snoke, 2003), with a stability check and fault-plane variance estimator proposed by Hardebeck & Shearer (2002). 25 focal-mechanism solutions with at least 12 first-motion observations and a fault-plane variance less than 20° were found. The focal mechanism seem to indicate that the sinistral Saalach Fault Zone poses an important tectonic boundary condition in the Mt. Hochstaufen area. Still active sinistral fault dispalcement may cause reverse faulting in a restraining bend at the south-eastern end of the Staufen Massif and normal faulting in the central part of the mountain chain. However, the number of derived focal mechanisms is not sufficient to give a definite answer to the question which tectonic processes control the seismicity of the Staufen Massif.

8   CONCLUSIONS

We have improved the location accuracy of the 2002 Mt. Hochstaufen seismicity by introducing a pseudo-3D-velocity model with topography and by using a probabilistic, non-linear location method. Additional improvement was achieved by analyzing wave-form similarities and relative relocation of groups of similar events.

The seismicity is mainly concentrated in the Staufen Massif and to depths less than 4 km. Several swarm-type earthquake sequences can be identified, which synchronously start with above-average rain events. A migration to depth can clearly be observed for the strongest earthquake swarm starting on August 8. This indicates that the seismic activity may be triggered by diffusion of rain water to seismogenic depth. Evidence for this hypothesis, based on our relocations, was recently reported by Hainzl et al. (2006) successfully predicting the seismic event rate from the calculated pore-pressure change at depth due to rainfall.

The derived focal mechanisms seem to indicate active sinistral displacement on the Saalachtal Fault Zone. Although, due to the small number of available focal mechanism a definite answer can not be given, this interpretation has to be tested carefully in the future and has major impact on seismic hazard assessment.

Relocation and focal mechanisms of rain-triggered earthquake swarms   15

Further improvement of the earthquake location and focal mechanism determination could be archived by improving the velocity model of the Mt. Hochstaufen area. This could be achieved by passive tomographic methods, however a denser seismological network would be as essential as a sufficient number of recorded earthquakes. Between April to September 2004, a dense network of 12 seismological station was installed around Mt. Hochstaufen. Additionally an earthquake swarm started in July 2005 synchronously with an intense rain event comparable to the one in August 2002. The data is currently analyzed and may help to identify the mechanism which drives the crust in the Staufen area so close to failure.

REFERENCES

Aster, C. R. & Rowe, C., 2000. *Automatic phase picking refinement and similar event association in large seismic datasets*, pp. 231–263, Kluwer, Amsterdam.

Bleibinhaus, F. & Gebrande, H., 2006. Crustal structure of the Eastern Alps along the TRANSALP profile from wide-angle seismic tomography, *Tectonophysics*, **414**, 51–69.

Bögel, H. & Schmidt, K., 1976. *Kleine Geologie der Ostalpen*, Ott Verlag Thun, Switzerland.

de Hoon, M. J. L., Imoto, S., Nolan, J., & Miyano, S., 2004. Open source clustering software, *Bioinformatics*, **20**(9), 1453–1454.

Deichmann, N. & Garcia-Fernandez, M., 1992. Rupture geometry from high-precision relative hypocenter location of microearthquake clusters, *Geophys. J. Int.*, **110**, 501–517.

16   *T. Kraft et al.*

Frisch, W. & Gawlick, H.-J., 2003. The nappe structure of the central Northern Calcareous Alps and its disintegration during Miocene tectonic extrusion - A contribution to understanding the orogenic evolution of the Eastern Alps, *Int. J. Earth Sci.*, **92**, 712–727.

Geller, R. J. & Mueller, C. S., 1980. Four similar earthquakes in central California, *Geophys. Res. Lett.*, **7**, 821–824.

Gephart, J. W. & Forsyth, D. W., 1984. Improved method for determining the regional stress tensor using earthquake focal mechanism data: Application to the San Fernando earthquake sequence, *J. Geophys. Res.*, **89**, 9305–9320.

Hainzl, S., Kraft, T., Wassermann, J., & Igel, H., 2006. Evidence for rainfall-triggered earthquake activity, *Geophys. Res. Lett.*, **submitted May 2006**.

Hardebeck, J. L. & Shearer, P. M., 2002. A new method for determining first-motion focal mechanisms, *Bull. Seism. Soc. Am.*, **92**(6), 2264–2276.

Kraft, T., Wassermann, J., Schmedes, E., & Igel, H., 2006. Meteorological triggering of earthquake swarms at Mt. Hochstaufen, SE-Germany, *Tectonophysics*, **accepted in May 2006**.

Lomax, A., Virieux, J., Volant, P., & Berge, C., 2000. Probabilistic earthquake location in 3d and layered models: Introduction of a Metropolis-Gibbs method and comparison with linear locations, in *Advances in Seismic Event Location*, edited by C. Thurber & N. Rabinowitz, pp. 101–134, Kluwer, Amsterdam.

LVG-Bayern, 2000. Digital elevation model DGM 5 (10 m grid), Landesamts für Vermessung und Geoinformation, Bayern, www.geodaten.bayern.de, Nutzungserlaubnis vom 6.12.2000, AZ.: VM 3860 B - 4562.

Matlab®, 2005. *The language of technical computing*, The MathWorks, Inc., Natick, Massachusetts, USA.

Menke, W., 1989. *Geophysical data analysis: Discrete inverse theory*, vol. 45 of **International Geophysics Series**, Academic Press, New York, USA.

Moore, E. H., 1920. On the reciprocal of the general algebraic matrix, *Bull. Amer. Math. Soc.*, **23**, 394–395.

Moser, T. J., van Eck, T., & Nolet, G., 1992. Hypocenter determination in strongly heterogeneous earth models using the shortest path method, *J. Geophys. Res.*, **97**, 6563–6572.

Munich Re Group, 2003. *topics: Annual review: Natural catastrophes 2002*, vol. 10th year, chap. The summer floods in Europe - A millennium flood?, pp. 17–25, Münchener Rückversicherungsgesellschaft, Munich, Germany.

Penrose, R., 1955. A generalized inverse of matrices, *Proc. Cambridge Philos. Soc.*, **51**, 406–413.

Podvin, P. & Lecomte, I., 1991. Finite difference computations of traveltimes in very contrasted velocity models: a massively parallel approach and its associated tools, *Geophys. J. Int.*, **105**, 271–284.

Poupinet, G., Ellsworth, V. L., & Frechet, J., 1984. Monitoring velocity variations in the crust using earthquake doublets: An application to the Calaveras fault, California, *J. Geophys. Res.*, **89**, 5719–5732.

Pujol, J., 2003. *Elastic Wave Propagation and Generation in Seismology*, Cambridge University Press.

Rietbrock, A. & Scherbaum, F., 1998. The GIANT analysis system (Graphical Interactive Aftershock Network Toolbox), *Seismol. Res. Lett.*, **69**, 40–45.

Rowe, C. A., Aster, R. C., Phillips, W. S., Jones, R. H., Borchers, B., & Fehler, M. C., 2002. Using automated,

high-precision repicking to improve delineation of microseismic structures at the Soultz geothermal reservoir, *Pure Appl. Geophys.*, **159**, 563–596.

Schwarzmann, A., Scherbaum, F., & Schmedes, E., 2001. *Erdbeben in Deutschland 1995. Berichte der deutschen seismologischen Observatorien mit einem Katalog wichtiger Weltbeben*, chap. Alpen - der Erdbebenschwarm im Raum Bad Reichenhall, pp. 29–36, Bundesanstalt für Geowissenschaften und Rohstoffe.

Snoke, J. A., 2003. *International Handbook of Earthquake and Engineering Seismology*, chap. FOCMEC: FOcal MEChanism determinations, pp. 29–30, Academic Press, San Diego.

Stammler, K., 1993. SeismichHandler – programmable multichannel data handler for interactive and automatic processing of seismological analysis, *Computers & Geosciences*, **19**(2), 135–140.

Tarantola, A., 2004. *Inverse problem theory and methods for model parameter estimation*, SIAM, Philadelphia.

Tarantola, A. & Valette, B., 1982. Generalized nonlinear inverse problems solved using the least squares criterion, *Rev. Geophys. Space Phys.*, **20**, 219–232.

Waldhauser, F. & Ellsworth, W. L., 2000. A double-difference earthquake location algorithm: Method and application to the northern Hayward fault, California, *Bull. Seism. Soc. Am.*, **90**(6), 1353–1368.

Weede, M., 2002. Die Geologie des Hochstaufen unter besonderer Berücksichtigung der Massenbewegungen, Diploma Thesis, Technical University of Munich.

Will, M., 1975. *Refraktions-Seismik im Nordteil der Ostalpen zwischen Salzach und Inn, 1970-1974; Messungen und deren Interpretation*, Ph.D. thesis, LMU Munich.

Wittlinger, G., Herquel, G., & Nakache, T., 1993. Earthquake location in strongly heterogeneous media, *Geophys. J. Int.*, **115**, 759–777.

Wolfe, C. J., 2002. On the mathematics of using difference operators to relocate earthquakes, *Bull. Seism. Soc. Am.*, **92**(8), 2879–2892.
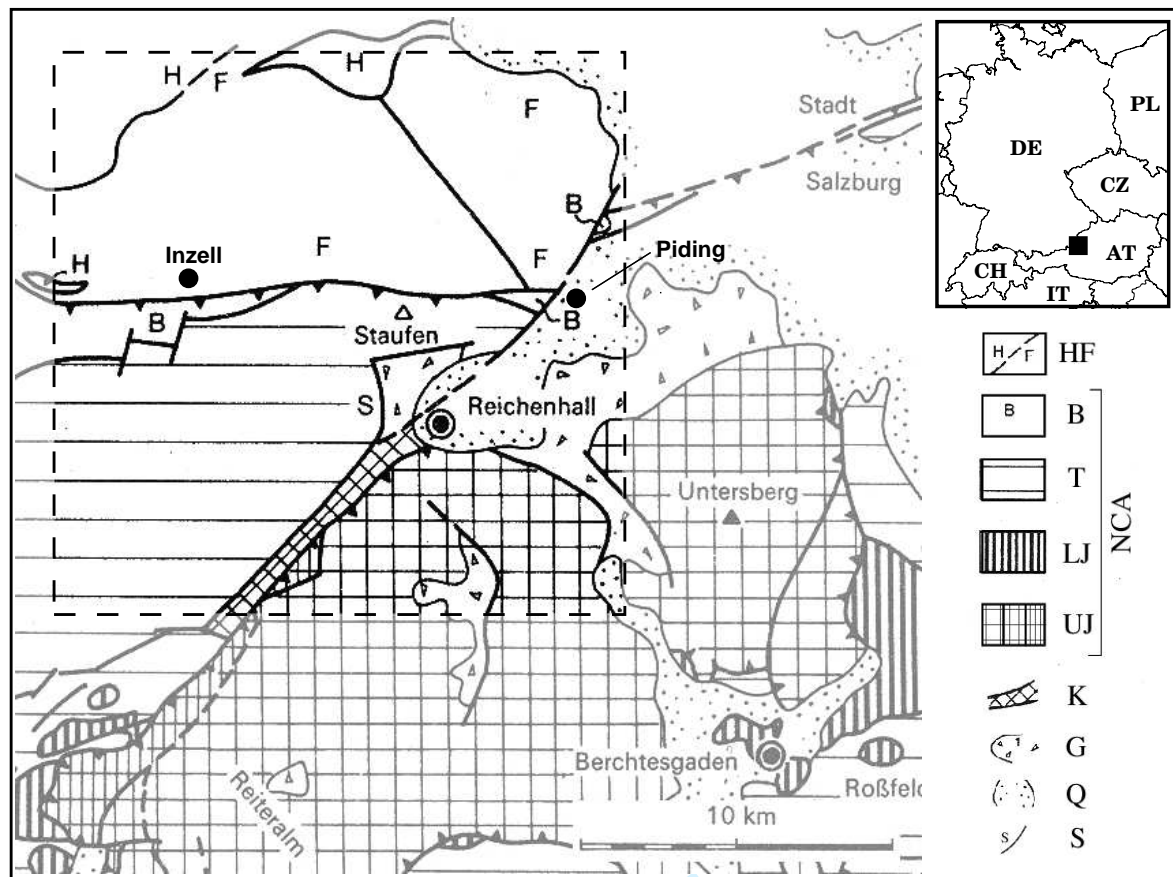
18   *T. Kraft et al.*

Figure 1. Tectonic map of the region around the study area (modified from Bögel & Schmidt, 1976). The classical subdivision of the Northern Calcareous Alps (**NCA**) in four nappe units is indicated. The study area is marked by a dashed square. The insert map gives the geographical location of the tectonic map. **HF** Helvetic Unit and Flysch Zone; **B** Bavaric, **T** Tirolic, **UJ** Upper and **LJ** Lower Juvavic Units; **K** Kugelbach Zone; **S** Saalach Western Fault; **G** Gossau conglomerates; **Q** Quaternary sediments.
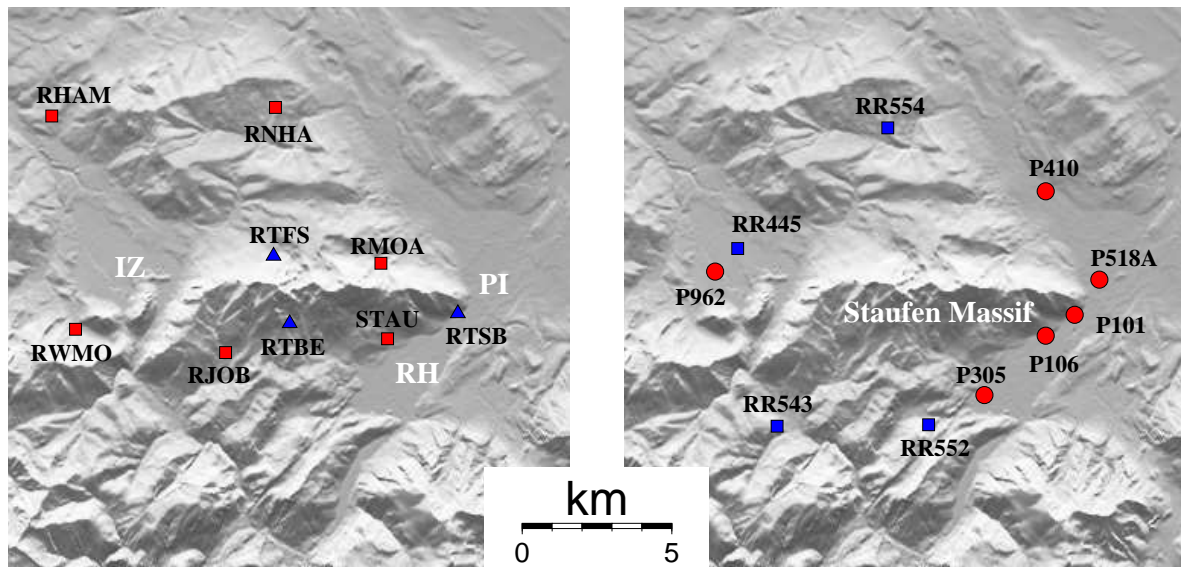
Relocation and focal mechanisms of rain-triggered earthquake swarms   19

Figure 2. Seismo-meteorological network around Mt. Hochstaufen. Map borders: lon. $12^o40'$ - $12^o57'E$; lat. $47^o40.5'$ - $47^o55.5'N$. **Left**: Map of permanent (squares) and mobile (triangles) seismological stations recording in 2002. Cities of Inzell (IZ), Piding (PI) and Bad Reichenhall (RH) are indicated. **Right**: Hydrological (circles) and meteorological (squares) stations.
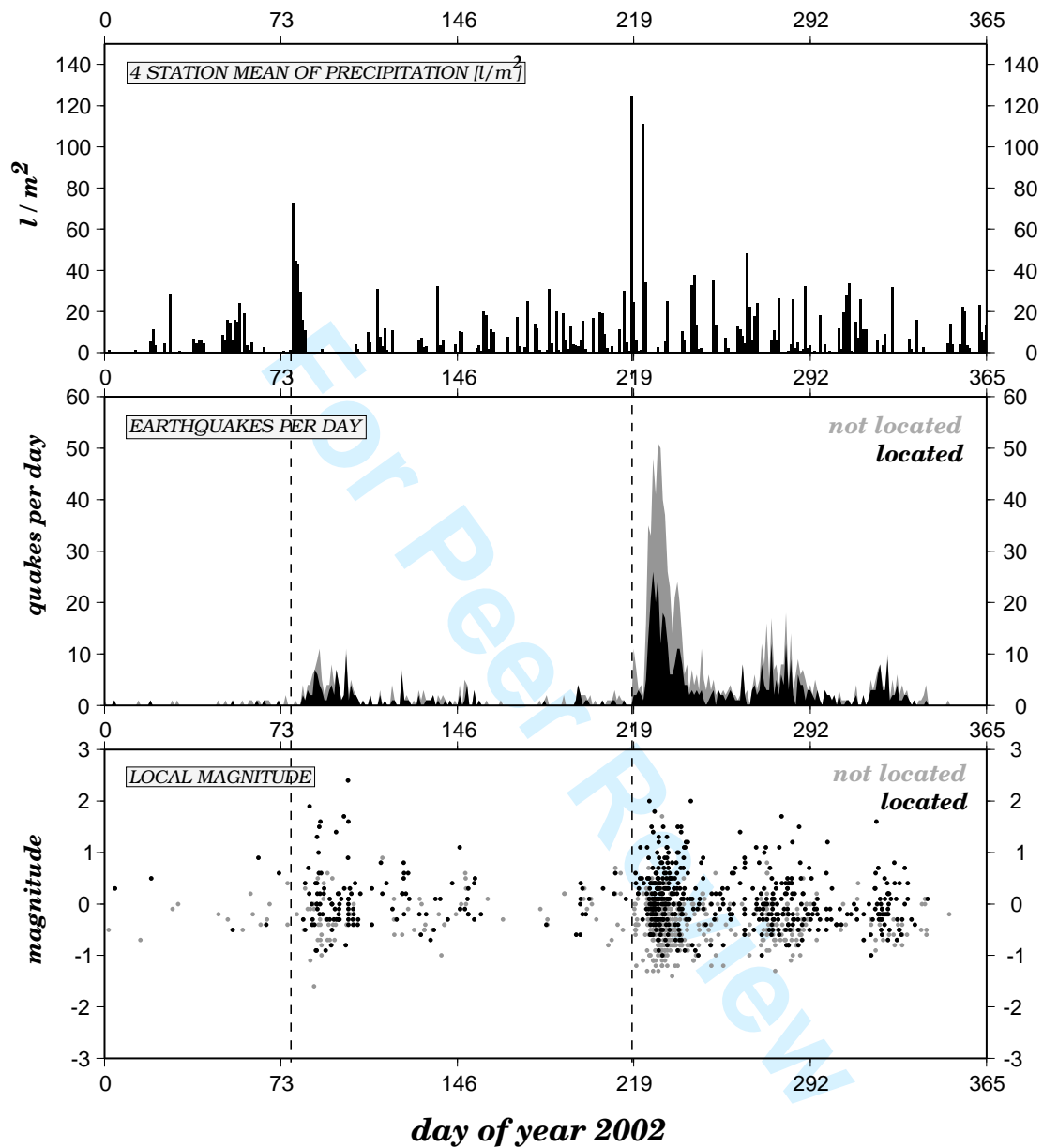
20   *T. Kraft et al.*

Figure 3. Spatio-temporal development of the seismicity in 2002. Vertical red lines mark the onsets of intense rain events in March and August. 612 located events (black), 559 not located events (gray).
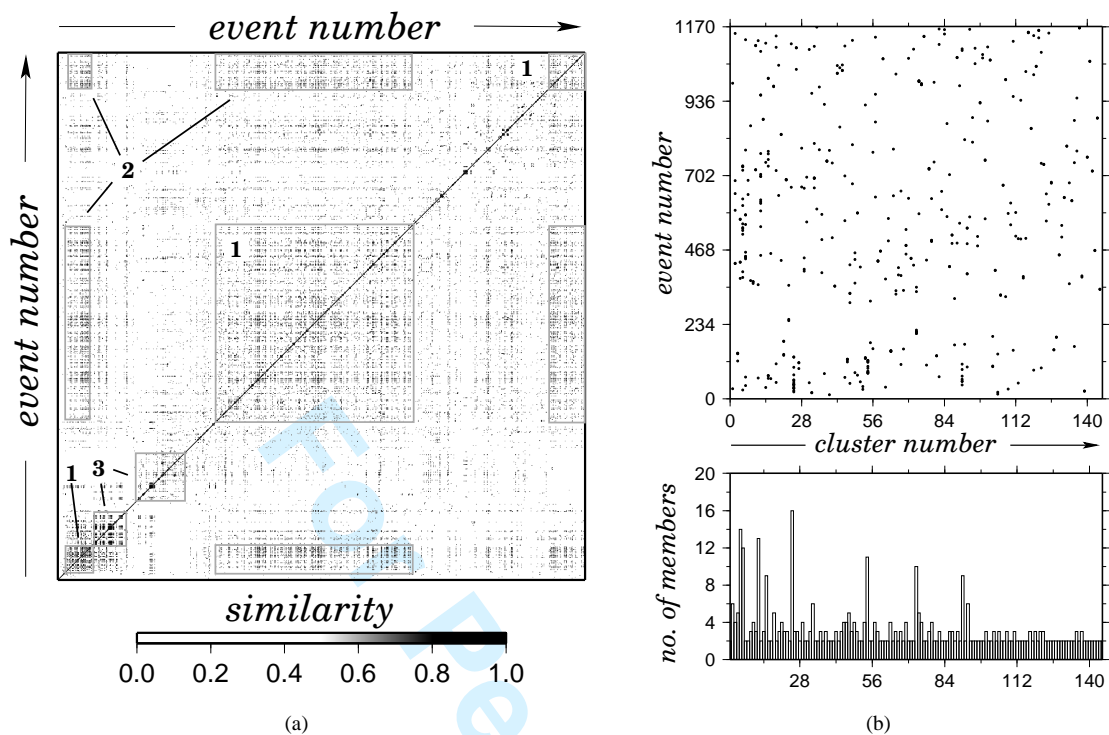
Relocation and focal mechanisms of rain-triggered earthquake swarms   21

(a)

(b)

Figure 4. a) Similarity matrix $\mathcal{C}$ for events in 2002 obtained from cross-correlation of STAU vertical seismograms. Gray scale indicates maximum cross-correlation coefficient. Event numbering is in temporal order. Highlighted areas and numbering corresponds to the discussion in the text. **b**) Clusters obtained from similarity matrix $\mathcal{C}$ by pairwise single linkage clustering with threshold $c_{ij} \geq 0.8$. Cluster numbering follows decreasing similarity. Top: Members of the 145 clusters. Bottom: Number of members per cluster.
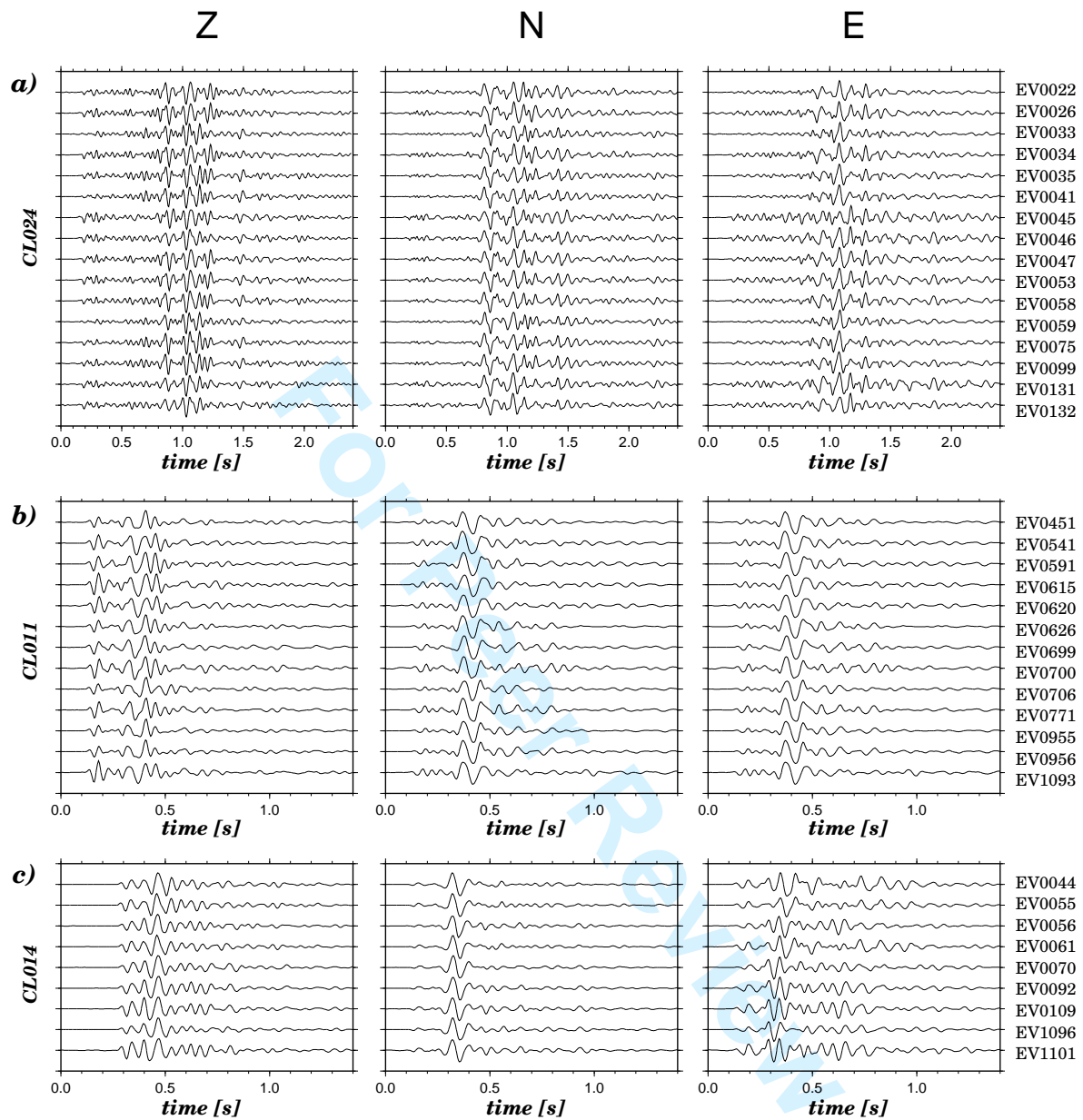
22   *T. Kraft et al.*

Figure 5. Example seismograms of station STAU form three clusters found in 2002. The clusters are representative of the March (CL024) and the August swarm (CL011 and CL014). The waveforms were bandpass filtered (3-20 Hz), scaled to maximum trace amplitude and aligned for maximum cross-correlation. Magnitudes can range from Ml=-0.8 to Ml=1.6 (CL014). For each cluster the three orthogonal components of ground velocity are shown (vertical: Z, horizontal: N = North, E = East). Please note the different window lengths in a), b) and c) given in seconds.

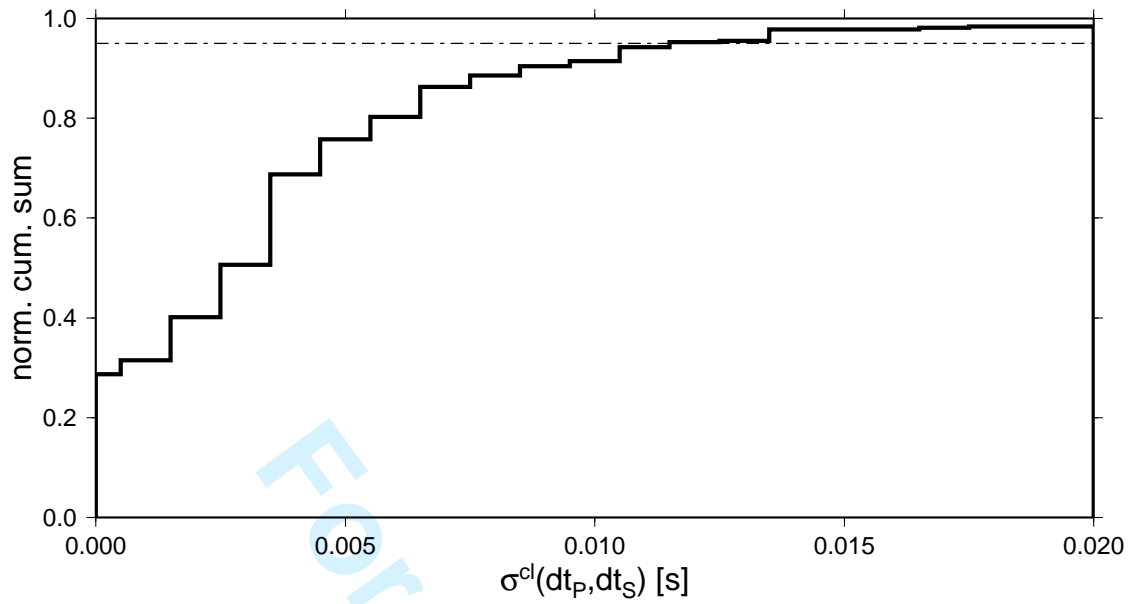*Relocation and focal mechanisms of rain-triggered earthquake swarms*   23

Figure 6. Normalized cumulative histogram of standard deviations $\sigma^{cl}(dt_p, dt_s)$ of the 314 analyzed sets of dt_p and dt_s from 51 clusters. As indicated by the dashed line, $\sigma^{cl}(dt_p, dt_s) \leq 0.012$ s holds for more than 95% of data.
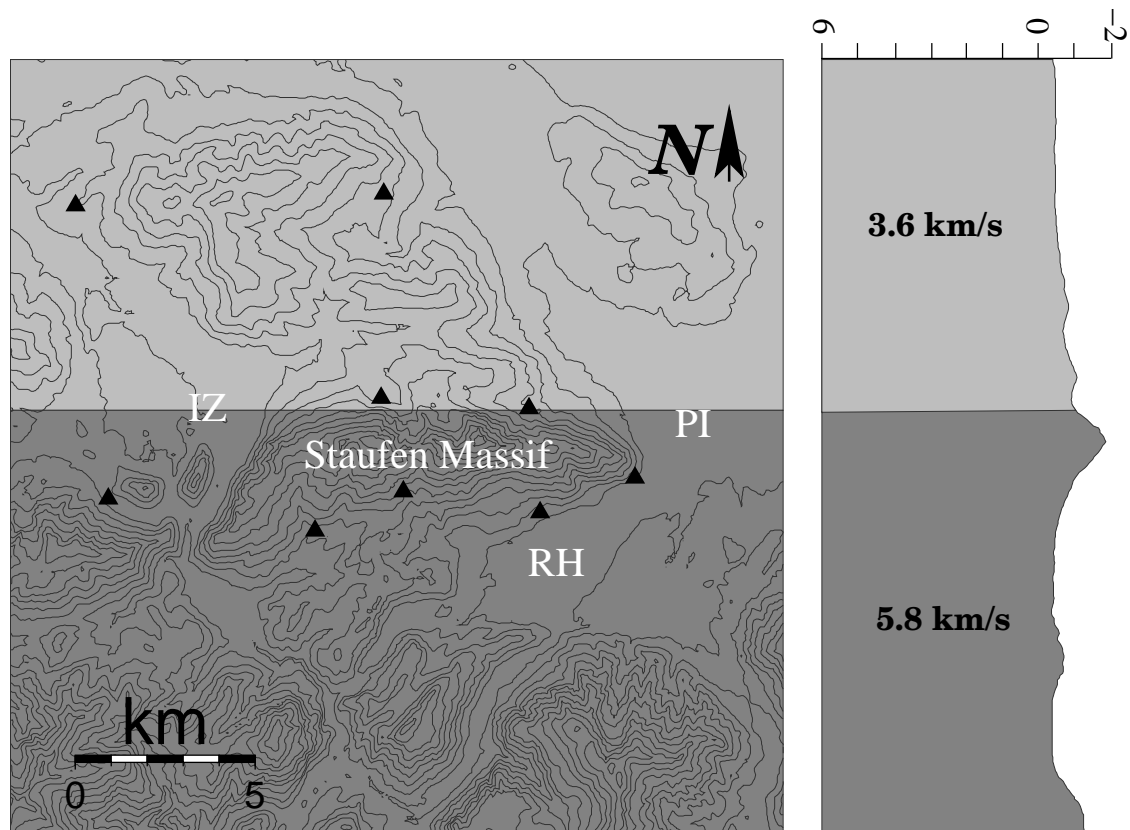
24 *T. Kraft et al.*

Figure 7. Pseudo-3D-velocity model with topography used for probabilistic nonlinear earthquake location. Velocities for the P-wave are given in the cross section. Seismological stations are indicated by triangles.
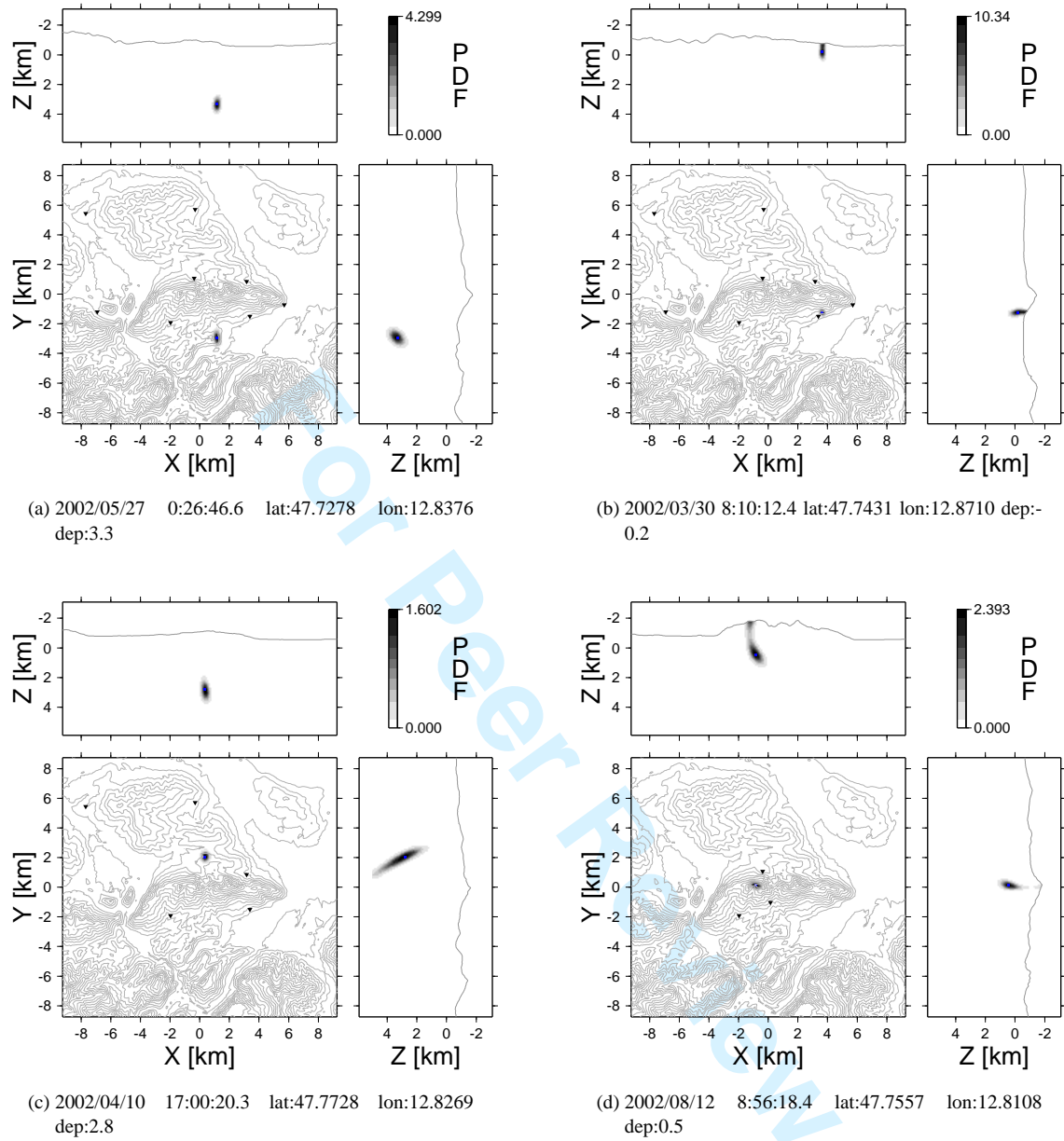
Relocation and focal mechanisms of rain-triggered earthquake swarms   25

(a) 2002/05/27   0:26:46.6   lat:47.7278   lon:12.8376
    dep:3.3

(b) 2002/03/30 8:10:12.4 lat:47.7431 lon:12.8710 dep:-
    0.2

(c) 2002/04/10   17:00:20.3   lat:47.7728   lon:12.8269
    dep:2.8

(d) 2002/08/12   8:56:18.4   lat:47.7557   lon:12.8108
    dep:0.5

Figure 8. Probabilistic location result for a) a representative event of the March swarm, b) the master event of cluster CL024 having the most members, c) the largest event Ml=2.4. d) Due to the non-zero velocity above topography, PDFs of badly constrained events tend to have a second maximum above the surface. These kind of events were excluded if the super-surface maximum was the maximum-likelihood point of the PDF.
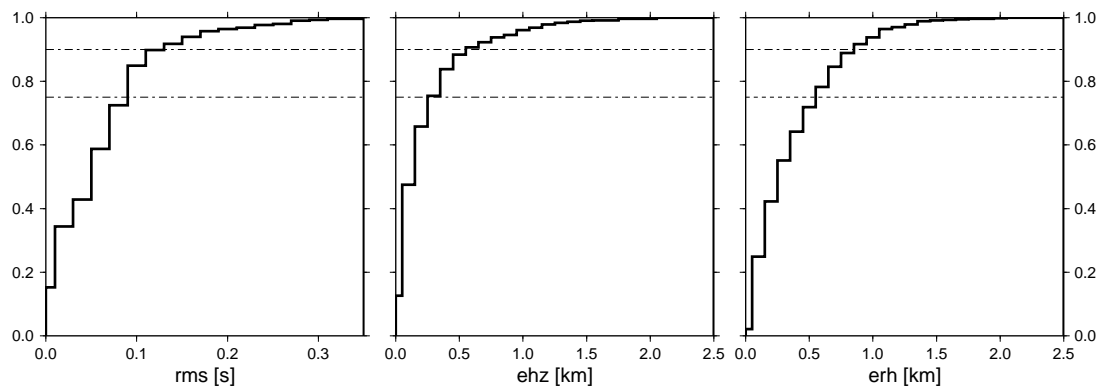
26   *T. Kraft et al.*

Figure 9. Error analysis of the probabilistic earthquake location. Normalized cumulative histograms of 67% confidence intervals of hypocenter depth (ehz), horizontal coordinates (erh) and root mean square arrival-time residual (RMS) are shown. As indicated by the dash-dotted lines, for 90% of the located events RMS < 0.12 s, ehz ≤ 0.6 km and erh < 0.7 km.

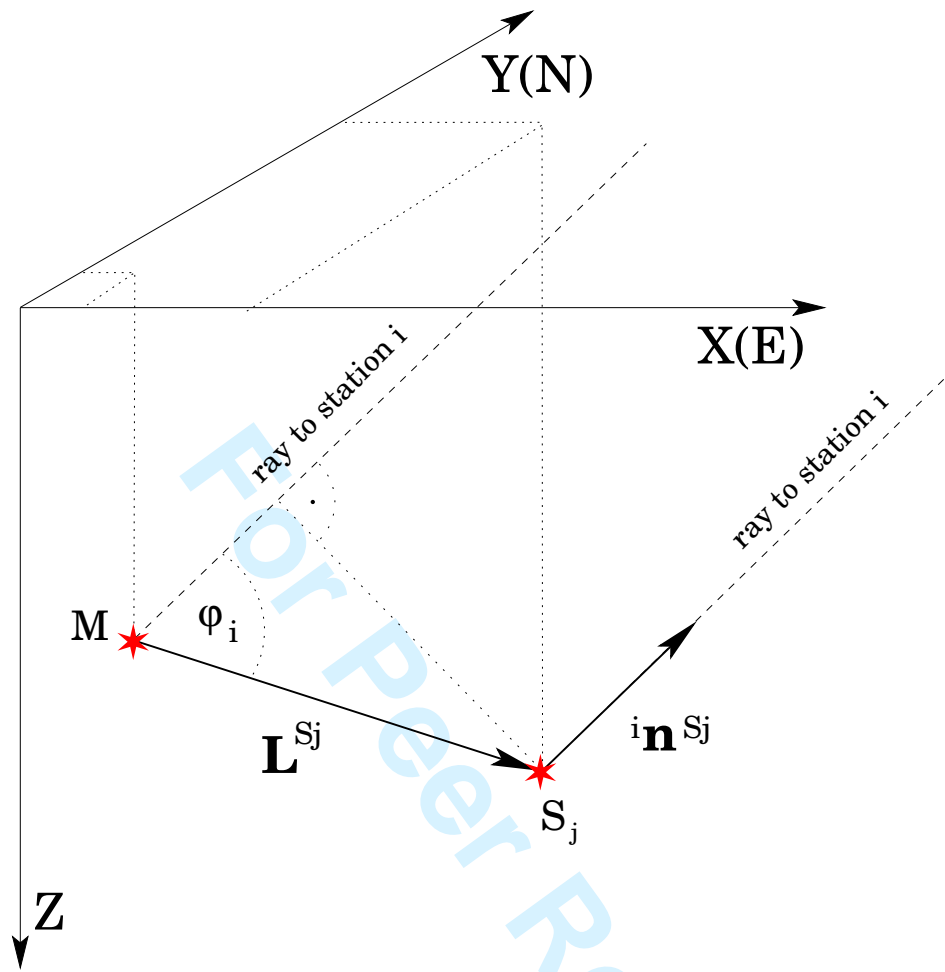**Figure 10.** Geometrical layout for master-event technique. **M**: maser event; **S**: slave event; $\mathbf{L} = (x, y, z)^T$: relative location vector; ${}^i\mathbf{n}$: unit vector pointing to station **i**.

28   *T. Kraft et al.*

(a) CL011

(b) CL024

(c) CL014

(d) CL142
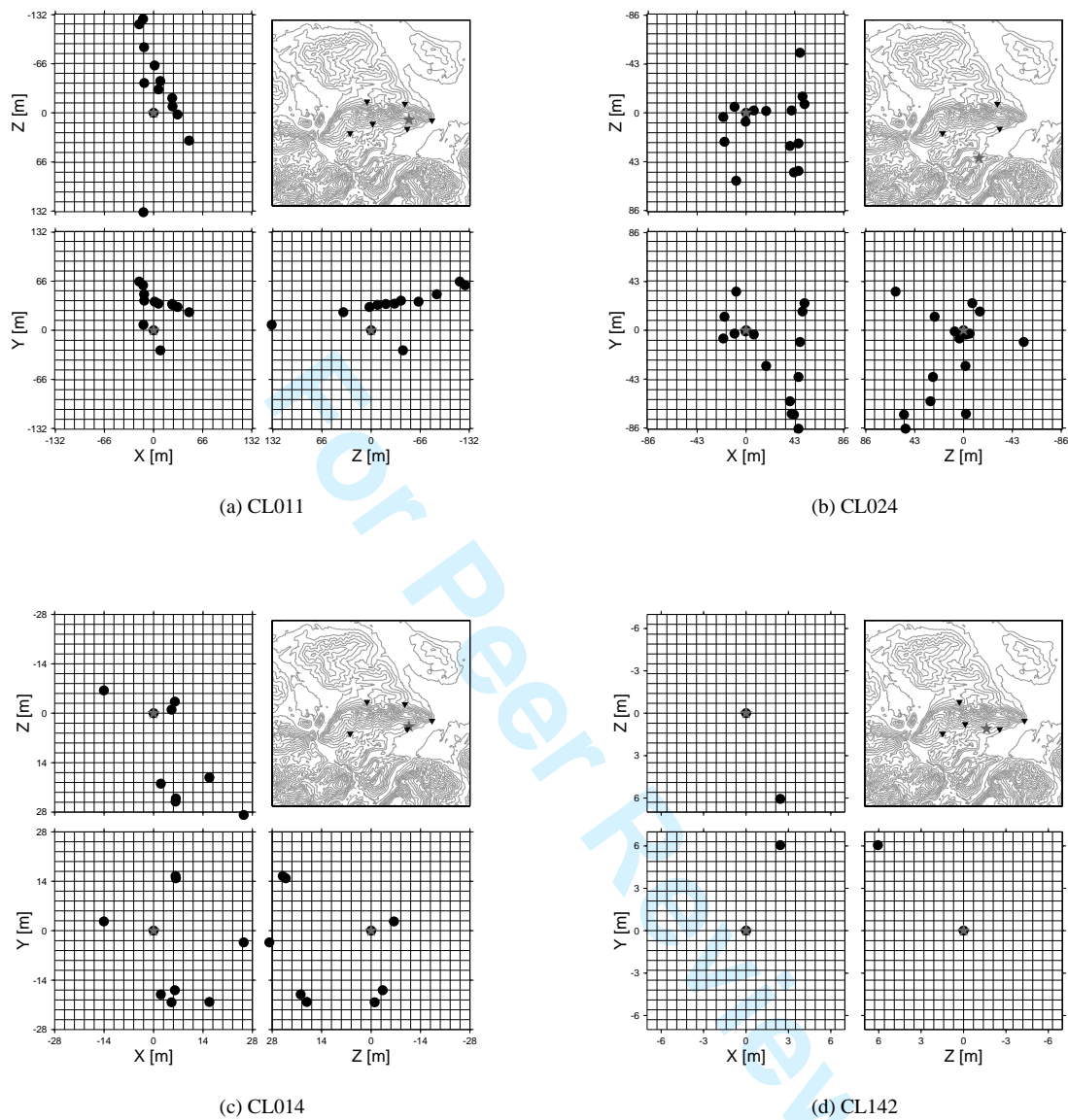
Figure 11. Relocation results for four clusters. Map-view and two vertical profiles centered on the master event (star) are shown. The absolute location of the masterevet and the available stations are indicated in a map of the study area in the top-right of the subfigures. Units are in meters from the master event. X: East-West, Y: North-South, Z: Down-Up (left handed system). a) CL011 b) CL024 most members (16) c) CL014 d) CL142 two-event cluster very small event distance.

Relocation and focal mechanisms of rain-triggered earthquake swarms 29
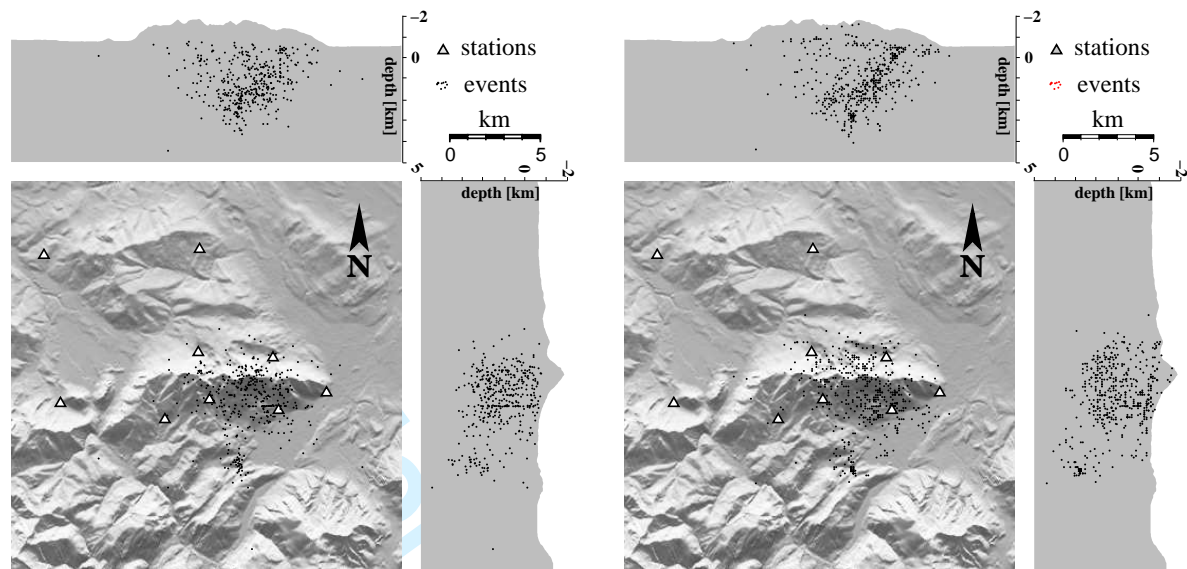
(a) Standard locations

(b) Relocated seismicity
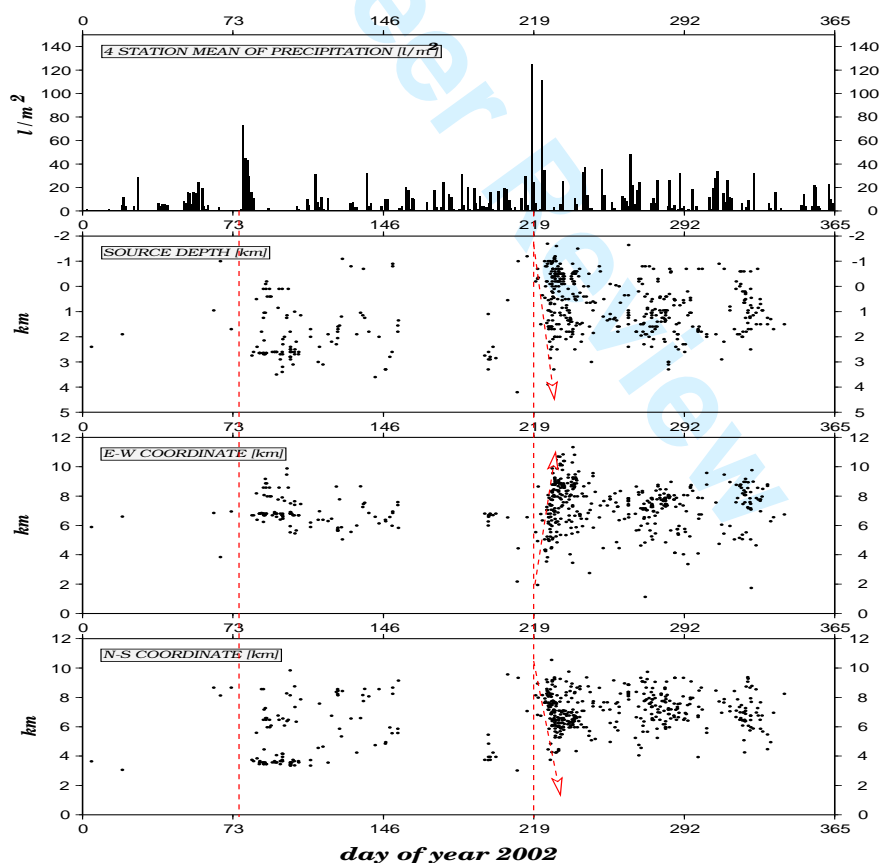
(c) Spatio-temporal development

Figure 12. Hypocenter map of 2002 Mt. Hochstaufen seismicity before (a) and after (b) relocation. EW- and NS-profiles through the summit of Mt. Hochstaufen are shown on top and to the left of the epicenter maps. The spatio-temporal development of the seismicity is shown in c). Dashed lines indicate the onset of the intense rain in March and August. Dashed arrows indicate the migration of the hypocenters.

30 *T. Kraft et al.*
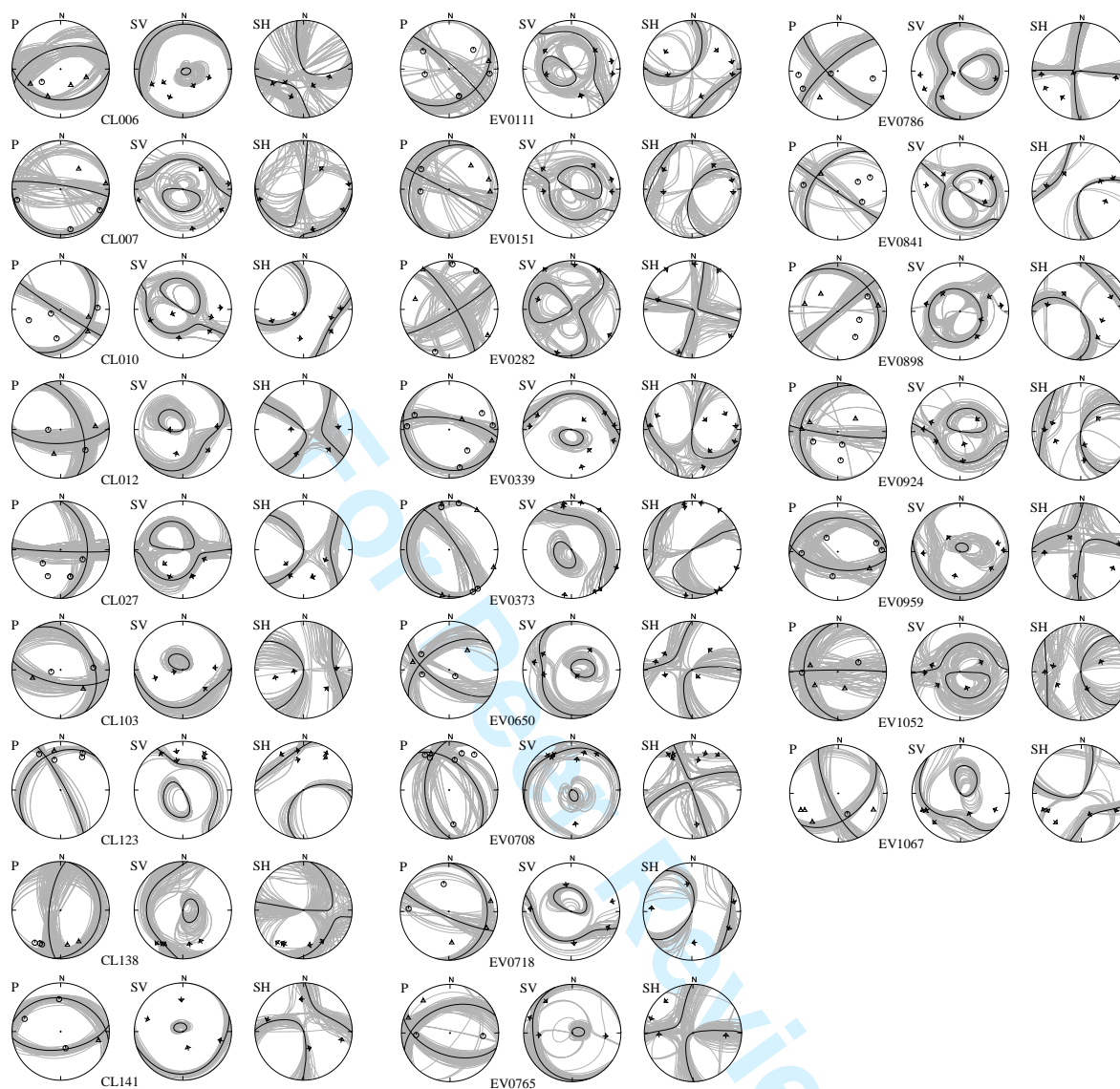
Figure 13. Focal mechanisms of earthquakes. 25 solutions with a minimum of 12 polarity observations and a maximum fault-plane variance of 20° are shown. Plots of the lower focal hemisphere contain nodal planes for P, SV and SH radiation for all derived solutions (light gray) and the preferred solution (black) for every cluster/event. Polarities are indicated for P (circle = up, triangle = down), SV (arrows: toward and away from source) and SH-component (arrows: to left and to right looking from source). Annotation indicates the individual cluster/event numbers.

Relocation and focal mechanisms of rain-triggered earthquake swarms   31

(a)

(b)
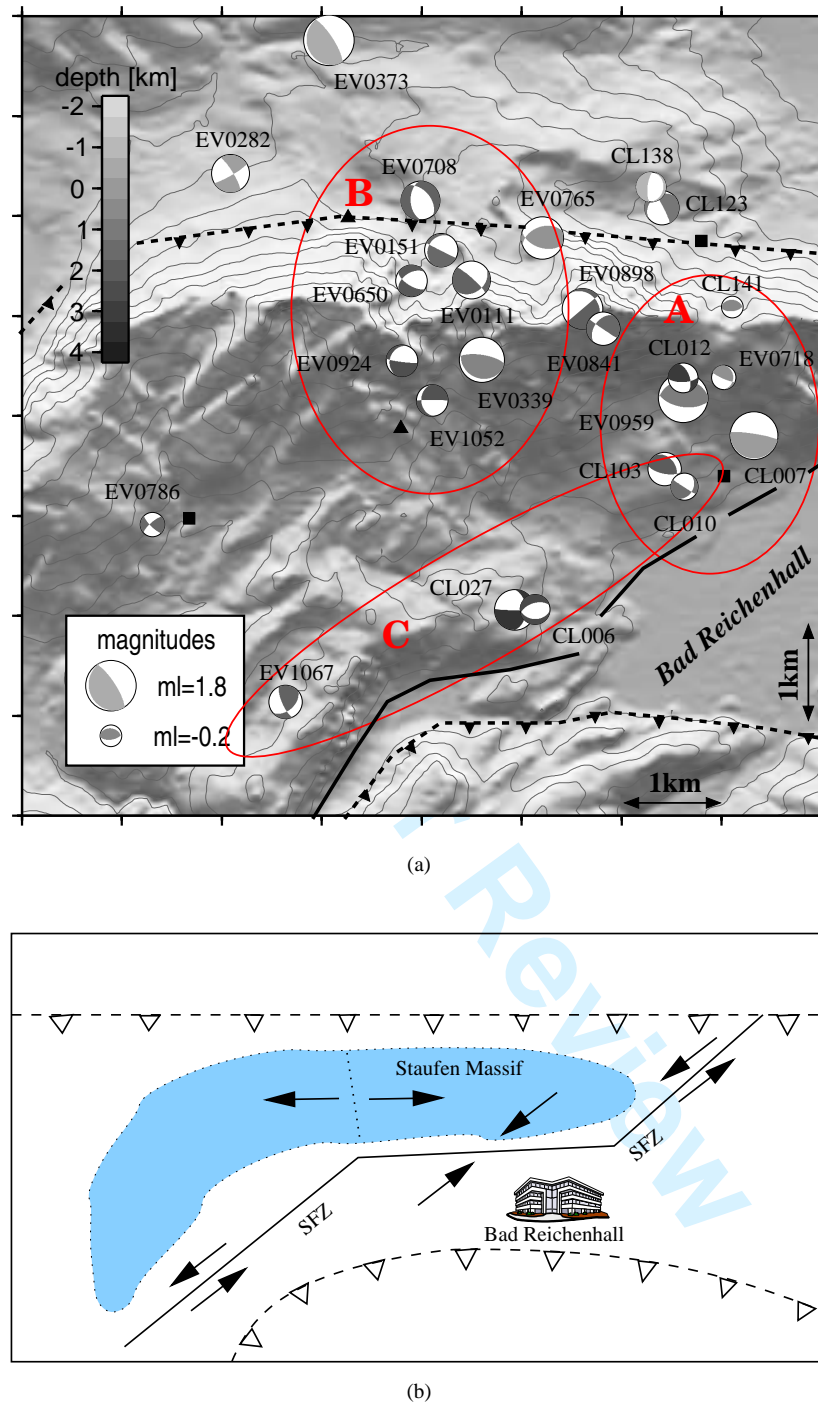
Figure 14. Epicenter map of the 25 derived focal mechanisms. a) Depth is indicated as gray scaled compressional quadrants of the focal mechanisms. Negative values correspond to altitude above sea level. The size of the beach balls is proportional to local magnitude. Source parameters of the clusters/events are given in Table 2. Three faulting regimes seem to exist and are indicated: (A) reverse, (B) normal and (C) sinistral strike-slip faulting. Major tectonic elements are taken from Frisch & Gawlick (2003): Saalachtal Fault Zone (SFZ, solid line), major thrust faults (dashed lines). b) Cartoon of a possible tectonic interpretation (see text).

W_{pick}	$\Delta t[s]$	δW_{pick}	c_{ij}	NonLinLoc
0	≤ 0.01			
1	≤ 0.05	$+0$	≥ 0.8	$\delta v = 0.2$ km/s
2	≤ 0.10	$+1$	≥ 0.5	$\Rightarrow \delta T = 0.05$ s
3	≤ 0.30	$+2$	≥ 0.3	(Moser et al., 1992)
4	≤ 0.60	$+3$	else	
5	≤ 2.00			$\Delta = 0.5$ km
6	else			

Table 1. Uncertainty/phase-weighting scheme for picking, cross-correlation and Nonlinloc Gaussian error estimation. Picking weights (W_{pick}) assigned according to picking uncertainty Δt. Cross-correlation phase weights were derived by incrementing (δW_{pick}) the picking weight of the master phase according to the cross-correlation value c_{ij}. The values δT and Δ represent the travel time error due to velocity model uncertainty (Moser et al., 1992) and a correlation length corresponding to wavelength of real velocity variations (Tarantola & Valette, 1982). Both values are used by NonLinLoc to calculate the covariance matrix of the calculated traveltimes (Lomax et al., 2000).

Relocation and focal mechanisms of rain-triggered earthquake swarms 33

Name	Origin Time 2002 UTC		Hyopcenter lat. 47°	lon. 12°	dep.	ml	Focal Mechanism strike	dip	rake	var.	strike	dip	rake	var.
CL006	07.15.	23:20:21	43.67	50.41	2.6	0.4	253.00	55.00	-101.00	±17	91.72	36.48	-74.76	±15
CL007	11.15.	08:31:35	44.59	52.18	-0.1	1.6	279.00	83.00	91.00	±17	90.85	7.07	81.91	±12
CL010	08.24.	22:08:48	44.32	51.62	1.4	0.2	123.00	87.00	-125.00	±7	28.73	35.11	-5.22	±6
CL012	10.11.	06:19:55	44.91	51.62	3.1	0.4	340.00	55.00	151.00	±11	87.64	66.60	38.68	±11
CL027	05.27.	00:26:46	43.67	50.25	3.3	1.1	92.00	87.00	-134.00	±8	358.90	44.08	-4.31	±8
CL103	08.19.	16:18:09	44.42	51.46	2.0	0.6	330.00	33.00	134.00	±10	100.97	66.93	65.72	±10
CL123	09.21.	19:16:58	45.83	51.46	1.2	0.7	332.00	82.00	-116.00	±5	226.07	27.12	-17.78	±6
CL138	08.15.	21:25:27	45.94	51.38	-0.9	0.4	186.00	71.00	-91.00	±14	9.07	19.03	-87.10	±16
CL141	10.22.	00:40:55	45.29	52.02	0.6	-0.2	281.00	32.00	106.00	±8	82.32	59.38	80.23	±5
EV0111	04.10.	16:53:47	45.45	49.93	1.8	0.9	312.00	82.00	123.00	±17	54.10	33.85	14.47	±13
EV0151	05.03.	22:56:07	45.61	49.69	1.6	0.6	211.00	22.00	-175.00	±16	116.36	88.13	-68.08	±16
EV0282	08.13.	04:41:08	46.04	48.01	-0.2	0.9	60.00	82.00	-169.00	±19	328.45	79.11	-8.15	±15
EV0339	08.14.	22:49:29	45.02	50.01	0.7	1.4	114.00	19.00	104.00	±8	279.23	71.58	85.24	±8
EV0373	08.15.	14:12:41	46.75	48.81	-0.6	1.8	327.00	76.00	86.00	±13	163.12	14.55	105.63	±11
EV0650	08.22.	14:58:43	45.45	49.45	2.1	0.5	237.00	49.00	-145.00	±10	122.33	64.35	-46.70	±11
EV0708	08.25.	12:27:54	45.88	49.53	1.8	1.0	320.00	48.00	-117.00	±11	177.29	48.54	-63.24	±11
EV0718	08.25.	21:36:57	44.91	51.94	0.3	0.0	0.00	22.00	155.00	±9	113.38	80.89	69.89	±8
EV0765	08.29.	09:53:55	45.67	50.50	0.2	0.6	108.00	52.00	116.00	±11	249.61	44.91	60.70	±11
EV0786	09.02.	22:10:38	44.15	47.36	1.6	0.0	135.00	76.00	165.00	±7	228.71	75.46	14.47	±8
EV0841	09.16.	14:31:50	45.18	50.98	1.6	0.6	124.00	88.00	136.00	±9	215.93	46.03	2.78	±7
EV0898	09.30.	15:48:09	45.29	50.82	1.9	1.1	230.00	90.00	113.00	±10	320.00	23.00	0.00	±10
EV0924	10.03.	03:43:21	45.02	49.37	2.4	0.5	200.00	25.00	-166.00	±11	97.27	84.13	-65.66	±13
EV0959	10.07.	01:40:27	44.80	51.62	0.9	1.7	267.00	31.00	80.00	±15	98.62	59.52	95.96	±13
EV1052	10.19.	13:05:17	44.80	49.61	2.3	0.5	270.00	87.00	-121.00	±16	175.02	31.13	-5.81	±18
EV1067	10.25.	16:33:52	43.18	48.41	1.7	0.6	50.00	47.00	157.00	±18	156.15	73.40	45.37	±8

Table 1. Source parameters of 25 events with a variance less then 20° of the fault-plane normals. For clusters the origin time of the master event is given. Hypocenter coordinates are given in minutes form 47° for latitude and from 12° for longitude. Depth is given in km b.s.l. Local magnitude (ml) is given for the master event or single event. For the preferred focal mechanism the orientation of the fault and auxiliary fault plane are given as dip, strike and rake in degrees following the convention of **?**). The variance of the fault-plane normals is given in degree for both planes. A epicenter map of this events can be found in Figure **??**a.